POLITECNICO DI TORINO
Repository ISTITUZIONALE

An experimental setup to study the collision force between brittle impacting bodies

(Article begins on next page)

05 February 2025

An experimental setup to study the collision force between brittle impacting bodies

Valerio De Biagi [a],*, Maddalena Marchelli [b]

[a] Department of Structural, Geotechnical and Building Eng., Politecnico di Torino, Corso Duca degli Abruzzi 24, Torino, 10129, Italy
[b] Department of Environment, Land and Infrastructure Eng., Politecnico di Torino, Corso Duca degli Abruzzi 24, Torino, 10129, Italy

ARTICLE INFO

ABSTRACT

A new experimental setup to study the interaction between two brittle bodies which can experience crushing, comminution or fragmentation during impact is herein presented. The system consists of a free falling body and an instrumented impacted plate, onto which an accelerometer is installed, lying on three force ring cells. The recorded acceleration is decomposed into Intrinsic Mode Functions thanks to a Variational Mode Decomposition technique to obtain relevant time-histories associated with specific vibration frequencies. The mass participating to each mode is obtained by comparing the discrete Fourier transforms of force and acceleration. Finally, the adoption of a high-speed camera provides additional insights into the interaction, in particular when non-spherical bodies are considered. The results of a small experimental campaign serving as a benchmark are presented and discussed.

1. Introduction

Impacts represent a major threat to structures, in particular when the they occur on load-bearing components [1–3]. Understanding how materials and structures behave under impact is essential to solving engineering problems. In frame-like structures made of slender elements, say beams, rods or columns, if the collision force generated by the impact is larger than the capacity of the element, a local failure happens, which, in turn, can propagate into a progressive collapse [4,5]. The impacts against plate-like elements, say slabs or walls, can cause local punching and penetration, with a consequent local failure of the element. Depending on the magnitude of the collision force, if the impacted element is not firmly fixed, its translation or overturning are also possible depending on several aspects, including the geometry of the impacted body [6]. Besides, there are some cases in which the impact causes larger damage in the impactor rather than on the impacted structure: this is the case when vehicles impact against bridge piers. This di-symmetrical nature of the phenomenon, i.e. a part experiences larger damage than the other, pushed structural engineers to classify the impacts based on the dissipative mechanism [7]. Although a clear position is missing, hard impacts can be associated to those in which the initial kinetic energy is dissipated by the striking object [8], rather than by the structure: this is the case of impacts of small vessels and vehicles that have deformable and energy absorbing parts in their layout. Soft impacts are those in which the initial kinetic energy is dissipated by

the impacted structure [8] rather than by the striking object: in this category the impact of projectiles or other rigid bodies is included [9].

The study of the response of a structure to an impact can be performed in three different ways: experimentally by replicating full- or scaled-impacts, numerically by simulating striking object and structure, or analytically on simple models that catch the behavior of the components of the system [7]. Experimental tests that replicate the real phenomenon in a controlled manner are useful and, sometimes, essentials: as examples, crash tests are fundamental to prove the effectiveness of the safety measures on a vehicle [10] or to show the effects of a falling rock against a protective shed [11,12]. Meanwhile, a detailed experimental campaign is time-consuming, expensive and a limited number of tests can be performed. Numerical models, say FE models, can quite well simulate the interaction between bodies in collision thanks to contact algorithms [13]. Discrete Element models can catch well fracture propagation phenomena that occurs in uniform bodies: as an example, Wittel et al. [14] performed numerical analyses on the processes involved in the initiation and development of fragmentation mechanisms when a brittle sphere impacts against a hard surface. Analytical models, say single or multi-degree-of-freedom systems, although they provide an effective tool for parametric analyses and extensive studies [15–18], suffer the fact that the interaction parameters must be appropriately determined, say the contact law must be included [19].

The impact is a dynamic phenomenon: inertia and strain rate effects on the material must be considered as their omission can largely

---

* Corresponding author.
E-mail address: valerio.debiagi@polito.it (V. De Biagi).

affect the response [20,21]. As an example, considering a part of a construction as the impacted structure, say a column, the facade or a slab, the brittle nature of concrete (or masonry), the presence of porosity in the material, and the presence of reinforcement modify the behavior of the system [22,23]. In this framework it has to be noted that concrete or masonry structures or, more in general, bodies which exhibit a brittle damage behavior, may experience localized surface damage, such as spalling, crushing, or the entire fragmentation of either the striking or the impacted body [24,25]. Experiments have shown that in brittle materials subjected to dynamic loadings, friction and crack propagation depend upon the loading rate, with a concordant trend between strength and loading rate. All such mechanisms presuppose a dissipation of energy [26], which has an effect on the impact features, say the duration and the maximum collision force, which are the engineering quantities required for assessing whether the impacted element resists.

Majeed et al. [12] have studied the time–history of the contact force between an impacting granite sphere and a concrete surface glued to a mass acting a single-degree-of-freedom system. The measure of the acceleration on the mass, coupled with a visual measurement of the displacement of the mass (via a high-speed camera) has allowed to define the time–history of the interaction force. The knowledge of the collision force generating during the interaction between brittle bodies, accounting for the local damage mechanisms, including the strain rate effects, occurring in such type of bodies, has several benefits. Firstly, a reliable prediction of the effects of the collision in analytical and numerical models by "tuning" the parameters of well established contact models, e.g. Hunt and Crossley [27,28] for specific collision types can be performed. Secondly, it would hypothetically foster new types of protection structures in which the impact energy is dissipated by fragmentation of the striking body rather than by other mechanisms [29], including failure of the impacted structure. This last point can be useful for such structures impacted by falling rocks [30], or in controlling (and stopping) pancake-type progressive collapse [31].

The present paper aims a describing an experimental device specifically designed to determine the time–history of collision force in presence of brittle damage on the colliding bodies. The need of a specific device derives from the fact that the current technology, except the case reported in Ref. [12], in which the impacting body has to be spherical, does not support the possibility of the striking body to exhibit damage. Considering specifically the impact test devices conceived to evaluate the time–history of the collision force, drop weight [32,33], pendulum [34], or horizontal hammer [35] devices have a load cell installed on the striking body between the steel head and the core mass, while the damage occurs on the impacted part [36]. This sensor setup does not allow to substitute the striking head with a brittle-like material since the possibility of the load cell to measure the force lies in the integrity of the striking head. In real impacts, the roughness of the surface and the position of the centroid of the impacting body with respect to the contact point play a relevant role in the evolution of the collision force. The current technology does not allow to measure the force during time at a laboratory scale and does not allows the impacting body to freely move during the collision, since it is firmly connected to the guides (as mentioned, in drop weight tests). To the knowledge of the Authors, full scale rockfall tests on real slopes are the only experiments in which a free falling body is released and the collision forces (with soil) are measured thanks to a triaxial accelerometer installed in the released body, coupled with high-speed cameras recordings [37]. The results in the impact tests can be compared with material and contact properties in the quasi-static tests and the contact law can be determined and implemented in either analytical or numerical FE models [12].

The present paper is organized as follow. In Section 2 the experimental setup is described. The interpretation of the data is reported in Section 3. Section 4 fully details the analysis of a sample experiment, while Section 5 reports a set of experiments specifically performed to illustrate the repeatability of the test and its effectiveness. Suggestions and hints for future work are proposed in the conclusions (Section 6).

Fig. 1. View of the impacted plate: the center of the 5 × 5 cm grid correspond to the centroid of the system.

2. Experimental setup

With the aim to study the collision between two fragile bodies, a system that does not constrain the impacting nor the impacted body was conceived and prototyped. The experimental setup consists in a target plate, illustrated in Fig. 1, in the following simply named as plate, lying over a concrete basement (plinth). A schematic of the experimental setup is proposed in Fig. 2. The plate is made of fiber-reinforced concrete (C25/30 premixed concrete with 0.75 kg hooked end steel fibers) to avoid reinforcement bars and is supported over three PCB Piezotronics Model M203B piezoelectric force rings (measurement range 88.96 kN, sensitivity 56.2 mV/kN, upper frequency limit 60 kHz) disposed at the vertices of a 20 cm side equilateral triangle. The adopted force sensors, onto which a confinement force must be applied, are suitable for impact measurements due to their extremely short rise time. The force sensors are located in such a way that the geometric center of the equilateral triangle corresponds to the vertical projection of the centroid of the plate. The system lies over a concrete plinth anchored to the floor. The bilateral connection between the plate and the support is guaranteed thanks to M12 screws that pass across the plate and the force ring sensors. A low-friction washer is installed over the sensor to homogenize the force on it. As requested by the system, a 15.3 kN confinement force on each load cell is guaranteed as the M12 screw is tightened at a torque of 37.5 Nm. In addition, a uni-axial Wilcoxon 732 A high frequency piezoelectric accelerometer (500 g peak, sensitivity 10 mV/g, resonance frequency 60 kHz) is installed on the bottom face of the plate in its geometrical center (Fig. 2) thanks to a 10–32 screw (that fits the tapped hole of the accelerometer) glued to the plate with an epoxy resin. The installation on the bottom face protects the accelerometer from the falling body. The three force sensors, plus the accelerometer, are connected with a low-noise coaxial cable to a 8-channels HBM QuantumX Data Acquisition System controlled by a PC. The test is recorded with a Photron Fastcam Nova S12 (monocrome) high-speed camera equipped with Zeiss Milvus 85 mm f/1.4 lens at 10,000 fps.

The plate can be impacted by a falling body which is released from a platform lying above at a predefined distance. The body is kept aside the plate before its release thanks to an electromagnetic actuator and a washer glued on it, as can be seen in the side view sketch of Fig. 2. The size of the body depends on the capacity of the electromagnet. Thanks to fact that the body is kept in position with a washer, complex geometries are possible. The platform can be
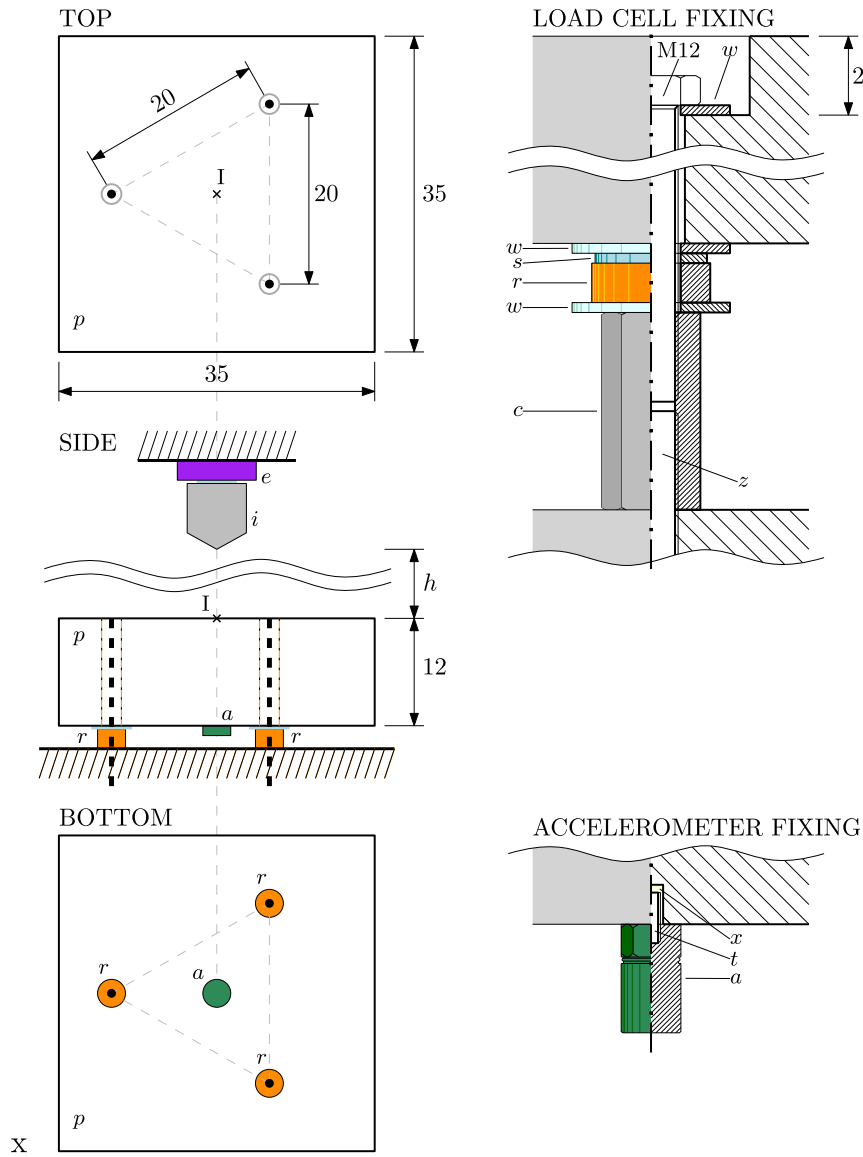
Fig. 2. Schematic of three views of the target plate and details of sensors' installation. Point I corresponds to the contact point, *a* to the accelerometer, *r* to the force rings, *p* to the target plate, *e* to the electromagnetic actuator, and *i* to the falling body. Blue lines refer to the washers and the black dashed line to the M12 connectors. Referring to details of the fixing: *w* is the mild steel washer, *s* is the special low friction washer, *c* is the hex rod coupler nut, *z* is the M12 bar embedded in the plinth, *t* is the 10–32 screw, and *x* is the epoxy resin. The sizes (in centimeters) refer to the sample test described in Section 4.

tilted in such a way that the orientation of the impacting body can be further modified. The position of the electromagnet on the fixed platform can be modified in such a way that the expected impact point coincides with the geometrical center I of the top face of the plate, which corresponds to the centroid of the plate. For this reason, a regular grid is drawn on the top part of the plate and its geometrical center is clearly marked (Fig. 1). The voltage in the electromagnet is measured by the acquisition system.

The powered electromagnet keeps the falling body in its position; once the power in the electromagnet is shut off, the body is released and starts its free fall. The release of the body serves as trigger for the high-speed camera and the QuantumX which simultaneously measures the voltage in the piezoelectric sensors (force rings and accelerometer) at a sampling frequency of 38.4 kHz. At the instant of impact, i.e. $\sqrt{2h/g}$ after the release, the free falling body reaches a velocity equal to $\sqrt{2gh}$, where *h* is the falling height measured from the top of the target plate to the bottommost point of the impacting body, see Fig. 2. As the impacting body is not constrained to any device, impact attrition, material comminution, and fragmentation processes can occur, as suited.

As depicted in the sketch of Fig. 2, the experimental setup presupposes that all the following entities are aligned (from top to bottom): (i) position of the impact point on the target plate; (ii) center of mass of the target plate; (iii) centroid of the bearing supports, i.e. the three force ring cells; (iv) vertical accelerometer.

During the impact phase, the dynamic equilibrium along the vertical direction holds:

$$F_I(t) + F_D(t) + F_E(t) = F(t). \tag{1}$$

where F_I is the inertia component, F_D and F_K are the components that originates from the damping and the elastic stiffness of the plate and connections. The $F(t)$ is the contact force between the impacting body and the plate, hence the collision force. Although previous studies indicate that the damping can be neglected during the impact phase, which generally lasts a couple of milliseconds [38], the term $F_D + F_E$ is the sum force recorded by the three load cells F_R. Hence, Eq. (1) can be rewritten as:

$$F_I(t) + F_R(t) = F(t). \tag{2}$$

After the impact phase, i.e. when there is no contact between impactor and target, the system enters in the free-damped vibration regime and the right-hand side of Eq. (1) is null. The weight of the impacting body is measured before and after the experiment to assess the amount of material that has been lost during the impact.

3. Interpretation of the records

The supporting system of the plate has an inherent stiffness that depends on the force rings and the M12 screws, and their connection to the base. Once impacted, the plate exhibits a complex dynamics that involves several vibration modes as it has a flexibility, although limited. It should be pointed out that the configuration of the supports, their stiffness, and the position of the accelerometer affect the capabilities of the system. In the current configuration the accelerometer installed on the bottom records the contribution of the vibration modes that have not a nodal line passing in or close to the center of the plate, where the accelerometer is located. Hence, there are modes that are not considered in the analysis.

To interpret the data according to the model of Eq. (2), the inertia component F_I cannot be considered as the mere product of the total mass of the plate times the recorded acceleration. This would lead to an error since the participating masses differ mode by mode. It is thus necessary to decompose the time–history of the acceleration to consider the various vibration modes and their participating masses. Several approaches to decompose a signal into modes are available in the literature to achieve such goal. The Empirical Mode Decomposition proposed by Huang et al. [39] decomposes the signal into principal Intrinsic Mode Functions (IMFs) by recursively defining the lower and upper envelopes of the extremes and removing the average. An IMF is an amplitude-modulated-frequency-modulated signal in the form:

$$\ddot{x}_i(t) = A_i(t) \cos\left[\phi_i(t)\right], \tag{3}$$

where the amplitude A_i and the instantaneous pulsation $\omega_i(t) = \dot{\phi}_i(t)$ are greater than zero, and their variation with respect of time is much slower than the phase $\phi_i(t)$ [40]. In this sense, the acceleration $\ddot{x}(t)$ can decomposed in functions and can be rewritten as:

$$\ddot{x}(t) = \sum_{i=1}^{n} \ddot{x}_i(t) + r(t), \tag{4}$$

where $r(t)$ is the residual.

The Empirical Mode Decomposition method suffers the fact that the instantaneous frequency of the obtained modes can largely differ from to the frequencies observed in the free-damped vibrations phase and can abruptly change. Recently, Dragomiretskiy and Zosso have formulated a new procedure, called Variational Mode Decomposition (VMD), to obtain the set of IMF based on an optimization process under the request that each IMF is chosen to be bandwidth in spectral domain [41]. In practice, each mode is mostly compact around a center pulsation ω_i which is to be determined along with the decomposition [41]. The approach is useful for the analysis of the recorded acceleration as the quality of its decomposition can be assessed in terms of the obtained central frequencies. This solution was found to be appropriate to perform the interpretation of the measured accelerations to obtain the time–history of the inertia $F_I(t)$.

A mass can be associated to each vibration mode of the system involving a vertical movement of the center of the plate, i.e. the participating mass, which is a fraction of the total mass. The vibration modes are related to the stiffness of the elements, the distribution of the masses, and the supports. To evaluate the participating mass of each vibration mode, the phase of the impact where $F_I(t) + F_R(t) = 0$ is considered. Hence, the acceleration and total force related to the free-damped vibration are compared in the frequency domain. The power spectral densities of acceleration and total force, PSD_a and PSD_F
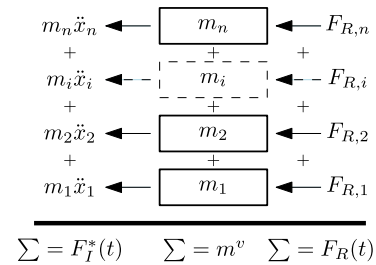

Fig. 3. Scheme of the participating masses and the reconstructed inertia $F_I^*(t)$.

respectively, are computed thanks to a Fast Fourier Transform (FFT) algorithm, resulting in:

$$\text{PSD}_a = \text{PSD}_a(f) \qquad \text{PSD}_F = \text{PSD}_F(f), \tag{5}$$

which are complex numbers. The mass m_i participating to a vibration mode with vibration frequency f_i can be intended as the ratio between force and acceleration, hence:

$$m_i = \frac{|\text{PSD}_F(f_i)|}{|\text{PSD}_a(f_i)|}. \tag{6}$$

Due to the regularity in the recorded signals, only the free-damped part of the vibration of the plate is considered for the estimation of the participating masses.

The reconstructed inertia F_I^* is the product of the intrinsic mode functions and the corresponding participating mass, i.e.:

$$F_I^*(t) = \sum_{i=1}^{N} \ddot{x}_i(t) m_i, \tag{7}$$

where $\ddot{x}_i(t)$ is the time–history of the ith intrinsic mode function of the acceleration. The scheme of Fig. 3 illustrates the idea behind the approach for $F_I^*(t)$ and $F_R(t)$. It should be noted that, due to the configuration of the supports and the position of the accelerometer, the sum of the participating masses is smaller than the total mass of the plate as there are vibration modes that do not presupposes a vertical movement of the center of the plate. It is anyway expected that the contribution to the dynamics of the system of the modes having a nodal line going through (or close to) the accelerometer position is very limited as the impact occurs vertically in the center of the system. Applying Eq. (2), the contact force $F(t)$ is obtained. It must be noted that the configuration of the sensors and the issues previously detailed involve an overestimation of the value of the contact force as the reconstructed inertia force, which is opposite in sign with respect to F_R, is underestimated. The uncertainty can be quantified by reconstructing the inertia force in the free-damped regime: the difference between the obtained force and the measured force is the vertical force due (i) to the higher vibration modes and (ii) to the modes that have a nodal line through the center of the plate.

4. Sample test

The sample test herein described considers as target a $35 \times 35 \times 12$ cm thick fiber-reinforced concrete plate (33.1 kg). The falling object consists on a 285.8 g, $5.2 \times 5.2 \times 5.2$ cm³ mortar cube released from a height of 1.40 m. The velocity at the impact is 5.24 m/s and the falling time is 534.2 ms. Fig. 4 details the time-histories of the acceleration (black) and total force recorded by the three load cells (blue) during a test. The time starts when the block is released. It is shown that the acceleration initially presents clean sinusoidal shape, that it is further disturbed by reflection of the shock waves along the sides of the plate (small perturbations of the signal); this trend is not seen in the records of the force. Following the test, the weight of the falling object was 285.6 g, hence 0.2 g were lost in the impact.
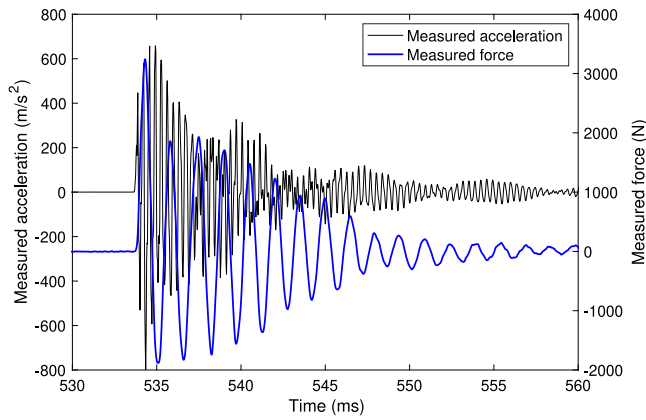
Fig. 4. Time-histories of acceleration and measured force during the drop test of a 285.8 g concrete cube falling from a height of 1.40 m.
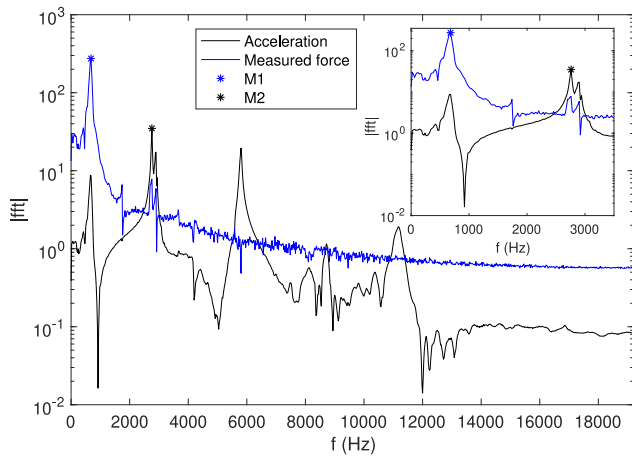
Fig. 5. Discrete Fourier transforms of the measured time-histories of acceleration and force in the free-damped vibrations part of the test, i.e. from 537.7 ms to 587.7 ms. The box provides a zoom of the results in the range 0–3.5 kHz.

The procedure described in Section 3 was implemented into a MATLAB script to obtain the contact force during the collision. The function *vmd*, already implemented in the programming platform, is used to apply the Variational Mode Decomposition algorithm. First, the participating masses were computed. Fig. 5 illustrates the power spectral densities of the recorded acceleration and force for the free-damped vibration part of the test from 537.7 ms to 587.7 ms. Referring to the recorded force, the peaks correspond to the following frequencies: 680, 2760 and 3660 Hz; referring to the acceleration, the peaks correspond to 680, 2760, 5800, 8720 and 11180 Hz. Each peak of the acceleration power spectral density corresponds to a vibration mode involving the vertical displacement of the central point of the plate. As expected, there are vibration modes that are not recorded by the force because either the participating mass is limited, or they do not involve vertical motion in the center of the plate where the accelerometer is located, i.e. they are specific flexural modes on the plate, only.

According to Eq. (6), the mass participating to each mode can be intended as the ratio between the power spectral densities of force and acceleration at a given frequency. With reference to the example here reported, we consider the following two frequencies: $f_1 = 680$ Hz and $f_2 = 2760$ Hz. For the first frequency, the magnitude of the discrete Fourier transform of the force is $|\mathrm{PSD}_F(680\,\mathrm{Hz})| = 273.88$ N, while the corresponding value for the acceleration is $|\mathrm{PSD}_a(680\,\mathrm{Hz})| = 8.81$ m/s². This means that the participating mass m_1 is:

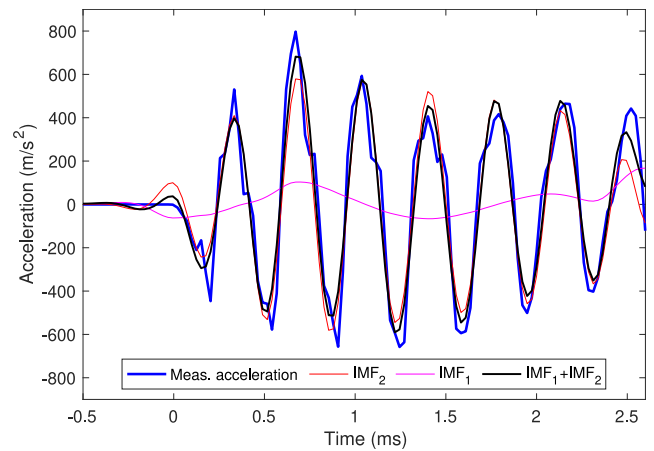$$m_1 = \frac{273.88}{8.81} = 31.08 \text{ kg}, \tag{8}$$

Fig. 6. Decomposition of the measured acceleration (blue) into implicit mode functions: the first two IMFs are plot, as well as their sum (in black). The zero time corresponds to the instant t_I.

representing the 94.1% of the total mass. Similarly, for the second frequency, the power spectral densities of force and acceleration are 7.78 N and 34.88 m/s², respectively, from which it results that the participating mass m_2 is equal to 0.22 kg. Higher peak frequencies exhibit participating masses that are considered negligible.

The mode decomposition reported in Eq. (3) was taken over a subsample of the entire recorded signal. In particular, considering that the impact begins when the acceleration first exceeds 1 m/s² threshold, corresponding to the instant t_b, the considered a subsample has bounds $[t_b\text{-}0.5 \text{ ms}; t_b\text{+}2.6 \text{ ms}]$. It results that two peaks of the recorded force are included. The Variational Mode Decomposition algorithm provides four IMFs and the residual; the IMFs with center frequencies close to f_1 and f_2, namely IMF$_1$ and IMF$_2$ are considered, only. Referring to the bounds of the subsample, it must be noted that the duration, i.e. the right bound, can be freely extended; on the contrary, the left bound is of primary importance for having a clear signal. The Authors adapted the bound so that IMF center frequencies were as close as possible to those used for the determination of the participating masses. Fig. 6 reports the impact analysis for the test previously illustrated in Fig. 4. It plots the acceleration in the subsample, the first two IMFs, along with their sum (in black). The obtained IMFs have central frequencies equal to 662.3 Hz and 2766.0 Hz, close to $f_1 = 680$ Hz and $f_2 = 2760$ Hz. The obtained frequencies are within a 5% error, defined as the limit threshold for which the decomposed signals are acceptable. For larger error, the subsample size and the number of IMFs must be modified. It must be noted that the mode decomposition remove the unwanted effects of the reflection of the shock waves on the sides of the plate as the vibration modes that are predominant in the free-damped part of the dynamics are taken into account, only.

Fig. 7 depicts the time-histories of the measured force F_R, i.e. the summed force from the load cells, and the inertia, reconstructed on the bases of the first two IMFs as described. For sake of clarity, the sign of F_I^* has been inverted. The inertia does not result null in the instants right before the impact, which is set at 0 ms, as the decomposition technique introduces an error at the beginning of the subsample. This represents one of the side effects of the method adopted to decompose the signal. At present, to the knowledge of the authors no better solutions are available as enlarging the subsample would not reduce the problem. The inertia component is larger than the measured force component up to 0.8 ms, when the two curves superpose. After 1.8 ms, as side effect of the use of mode decomposition techniques, which present the so-called end effect error [42] due to the sudden interruption of the data to be processed, the curves start to diverge. As signal reconstruction techniques found in the literature [43,44] are not
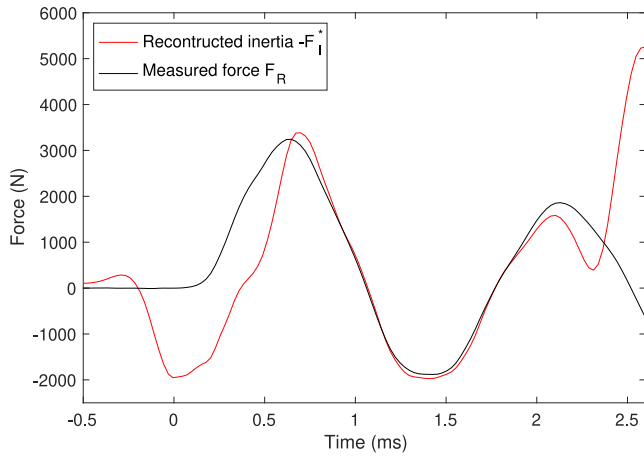
Fig. 7. Measured force (F_R) and reconstructed inertia (F_I^*). To highlight the superposed (but opposite) plots, the reconstructed inertia was multiplied by −1. The zero time corresponds to the instant t_b.
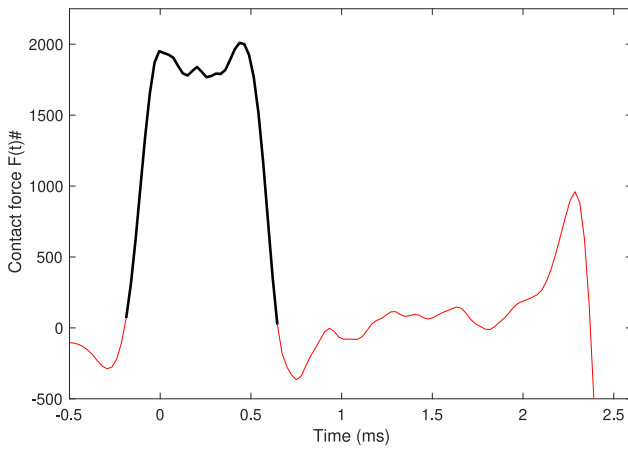

Fig. 8. Contact force as a result of Eq. (1). The zero time corresponds to the instant t_b. The curve is divided in three segments: the central black parts is considered as the contact force.

suitable due to the transient nature of the recorded signal, the Authors suggest that the subsample considered in the analysis extends (in time) after the impact not to include the end effect error in the reconstructed inertia.

Fig. 8 depicts the contact force as the sum of F_R and F_I^*. It is noted that the force is quasi-null when the two components can be superposed. Despite the side effects of the VMD, the Authors consider as contact force the positive part, only, i.e. the black part. The contact duration is 0.83 ms and the maximum force is 2050 N. It can be noted that the contact force has a sudden raise, followed by a plateau at ~1.8 kN and a sudden drop. The reconstruction of the inertia force in the free-damped part of the record shows that the maximum error on the maximum value of the force is about ±100 N. This value corresponds to the amplitude of the oscillation of the contact force plot in Fig. 8 from 1.1 to 1.7 ms, i.e. after the impact and before the raise of the end effect error in the decomposition.

5. Preliminary results

To assess the capabilities of the experimental setup, a preliminary test campaign was performed. Three set of tests are herein reported: (i) repeated tests with an elastic body (a tennis ball), (ii) tests with a concrete cube, and (iii) a sample test of a concrete over rock plate (gneiss) impact recorded by the high-speed camera.
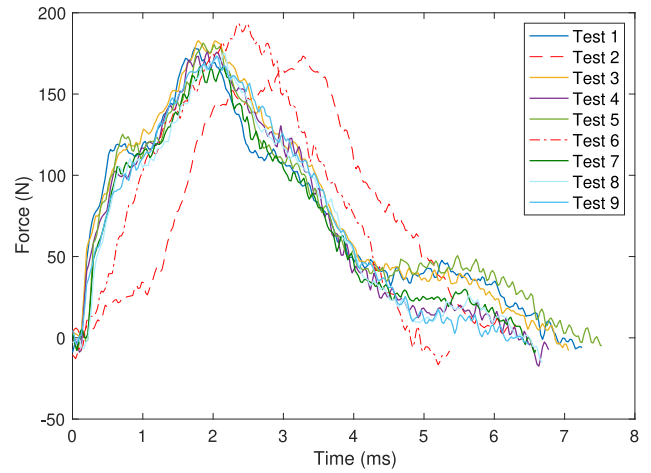

Fig. 9. Contact force time-histories for the nine tests performed with a tennis ball drop from a height of 1.440 m.

5.1. Repeated tests with a tennis ball

The repeated tests with a tennis ball as a falling body were performed with the aim of assessing the repeatability of the results. In such tests it was supposed that no damage on either the impacting body and the impacted plate would occur. The ferro-magnetic washer was held in position thanks to elastic bands. The tennis ball, which weight is 65.2 gr was released from an height of about 1.44 m. Nine tests were performed and the corresponding recorded signals were elaborated thanks to the procedure illustrated in Section 3. Fig. 9 depicts the time-histories of the contact force during the impact. It is seen that, 7 curves (colored) out of 9 can be easily superposed. The maximum impact force is between 150 and 175 N, while the duration of the contact is about 6.5 ms. The curves in red (dashed and dashed-dotted) are related to tests which results cannot be superposed to the others (i.e., 2 and 6). The non-superposition results from the fact that the peak of the force is delayed in the time, if compared to the colored curves. It is worth to note that, even for such tests, the maximum force and duration are compatible with those of the colored curves.

In the idea of the Authors, the replicability of the tests on the tennis ball must be related to: (i) the material behavior of the fallen object, which does not change from one test to the other, (ii) the spherical shape at the contact point, independently from the exact initial position at the release point. With the current knowledge, we argue that the difficulty of obtaining the correct value of the participating masses when the impact force is weak and the impact duration exceeds 4–5 ms is the reason for the odd behavior of tests 2 and 6. In such situation, the multiple reflections within the slab hide the relatively weak acceleration due to the vibrations, making the process complex. A correct evaluation solution was found for 7 out of 9 tests, showing that the device is not suitable to get the force time–history for low collision forces.

5.2. Repeated tests of concrete over concrete impact

Preliminary tests on concrete-over-concrete impact were performed to check the quality of the outputs and to assess the effect of a different initial position. In fact, although the efforts in putting the falling body in the same position, the current experimental setup does not allow an exact initial orientation. As a result, a variability in the response is expected since the position of the contact point differs test by test. Despite this variability is a consequence of the randomness in the initial orientation of a real falling object, it is not a real drawback but presupposes an aleatory uncertainty. Fig. 10 illustrates the force time-histories of three tests of a 5.2×5.2×5.2 cm^3 concrete cube impacting
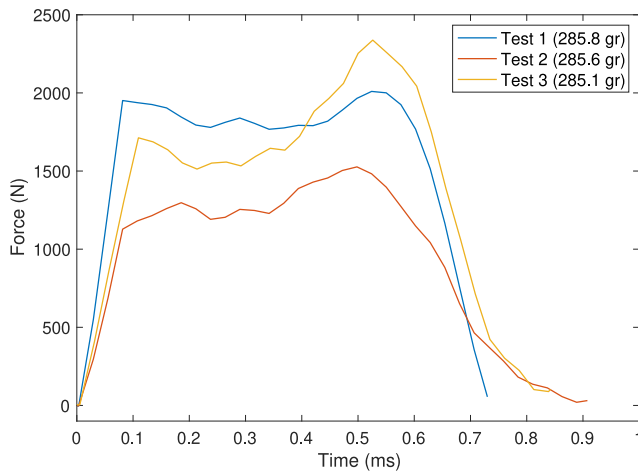
Fig. 10. Contact force time-histories of drop tests of 5.2×5.2×5.2 cm³ concrete cube falling from a height of 1.40 m.

against the concrete plate described in Section 2. The falling height is 1.40 m and the maximum force is between 1400 and 2350 N; it should be noted that the maximum contact force expected through the empirical formulae by Yong et al. [30] is 2435 N. The weight of the cubes was measured before each test. It is observed that the falling masses differ; the weight loss in tests 2 and 3 is due to the interface processes (such as comminution and release of small pieces of impacting body) occurred during the impacts 1 and 2.

5.3. Preliminary investigations with HS camera

To highlight the mechanisms that occurs at the impact, a set of tests was recorded with the high-speed camera. The basic analysis of the images, coupled with the measured forces and acceleration, allows to understand the physical processes that occur during the contact of rough and non-spherical bodies (at this preliminary stage, the synchronization between measures and camera was based on the images). To this aim, the concrete plate previously described was substituted with a rectangular-like shape rock slab (gneiss) with a mass of 49.5 kg. The sensors setup and plate arrangement were replicated (force cells and accelerometer) and the effectiveness of the setup was thoroughly checked with elastic impacts (tennis ball drops). Fig. 11 illustrates the time–history of a drop test with a 5.2×5.2×5.2 cm³ concrete cube (weight equal to 287.2 gr) falling from a height of 0.845 m. The contact lasts 4 ms and a variable contact force was obtained. Thanks to the high-speed camera, the curve was interpreted. The two peaks are associated to two distinct impact phases. The body arrives at the target slightly counterclockwise tilted (at time 0 ms). The first impact occurs on the left side and the body starts rotating. The maximum force is at around 1 ms when the body is in its horizontal position. Then, a second contact occurs (at 1.9 ms), corresponding to a new peak in the force time–history curve. After 1.9 ms the body rotates clockwise and starts its rebound. Thanks to the high-speed camera, the small (comminuted) parts of the falling body that are released during the impact can be clearly seen (in the red rectangles). It is noted that the crushing occurs during all the duration of the process, as highlighted by the ejected debris.

6. Discussion

In the standard drop impact tests performed with the already existing testing machines, the impacted body, which is the one that undergoes failure, is kept in position by supports. The configuration of such supports can modify the failure of the element as constraints
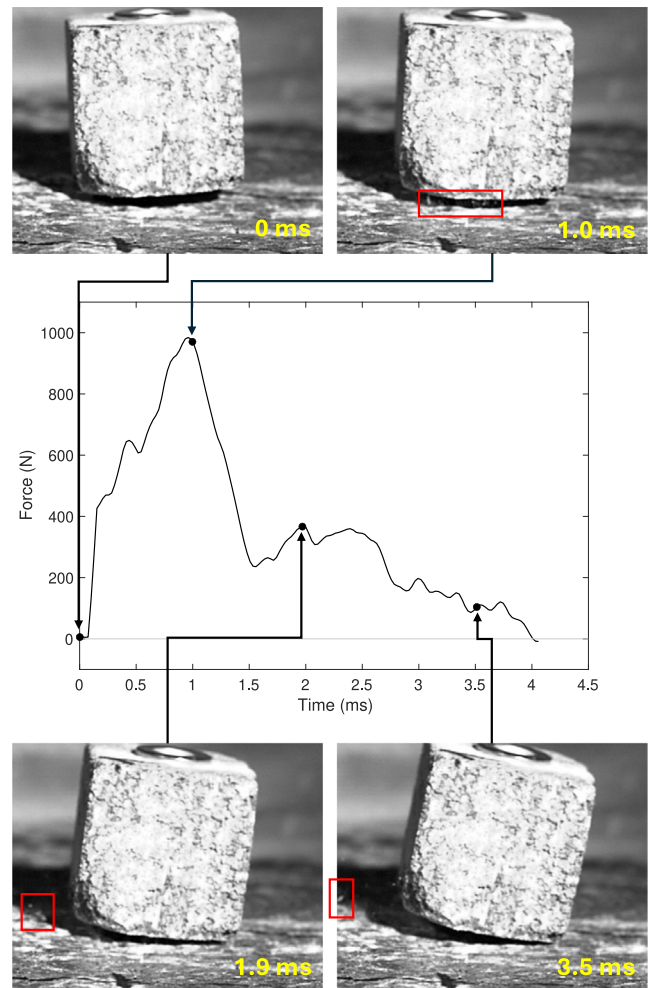

Fig. 11. Contact force time–history and corresponding frames obtained from the high-speed camera (10,000 fps). The red rectangular boxes show the debris created and ejected during the impact.

(that are not present in the real cases) arise. This point is relevant when dealing with bodies experiencing brittle failure, as the rupture can affect the entire body. As an example, the sphere-slab interaction force that generates the failure mechanisms numerically modeled by Carmona et al. [45] or those experimentally observed by Guccione et al. [46] cannot be measured with a standard drop impact test as the supporting system necessarily modifies the way the fracture propagates within the body. In a previous work, Wu et al. [47] tested the spheres with a double impact device, but achieving different fragmentation modes. The proposed device overcomes this limitation as it leaves the falling body free of any constraint.

Although some issues and limitations have been observed, preliminary tests have shown the repeatability of the results and the possibility to highlight complex interaction mechanisms when a high-speed camera records the experiment. In its present configuration, the device accounts for small falling objects, only. This is not a drawback as scaling laws can be implemented to simulate larger phenomena characterized by larger kinetic energy [48–50]. The problem of scalability emerges in brittle bodies, say in rocks, in which it is has been demonstrated that material strength is both size- and rate-dependent. In addition, fracture mechanics properties must be considered [51]. Oshiro and Alves [52] proposed, so far, a solution to the problem of non-scalability of structures under impact loads because of the strain-rate effects. Recently, tentatives on the definition of the scaling laws specifically tailored for problems with strain-rate [53] and fracture mechanics dependent materials have been formulated [54,55]. It is worth mentioning that

the time–history of the collision force can be back-analyzed and the parameters of the contact law can be obtained.

An ongoing experimental campaign on the effects of energy and shape would provide insights into the progressive damage of structures through pancake-type progressive collapse, which is characterized by the progressive downward impact of floors in multi-storey buildings [56]. The same experimental device can be used for the study of the interaction force between rock blocks in motion, e.g. in rockfall phenomena, and constructions, either in concrete or in stone/masonry, to be helpful for vulnerability studies [57].

7. Conclusions

A new experimental setup devoted to the analysis of the collision force that is generated by the impact of two bodies has been presented. The experimental device consists in a drop weight system with the falling body not connected to any driving device, hence free to move during and after the impact. The collision force is measured thanks to three load cells and an accelerometer. The recorded measures are interpreted thanks to a Variational Mode Decomposition technique which allows to reconstruct a simplified time–history of the inertia force based on the estimation of the participating masses. The system is versatile and suitable for the investigation of concrete, rock or masonry interactions as the impacted plate can modify in shape and material. Despite its adaptability is quite straightforward, the influence of the geometry, the position of the supports and accelerometer must be thoroughly checked when a different configuration is considered.

As detailed in the paper, the system is suitable to study the interactions that presuppose damage mechanisms that can be observed in brittle bodies, such as comminution, crushing or fragmentation. Besides, there are some limitations that must be considered when designing an experimental campaign and interpreting data: (i) the impact force must be strong enough to obtain a clear power spectral density plot of the acceleration in the free-damped regime to define the participating masses, and (ii) the measurement of the impact force must be accompanied by quantification of the error induced in the measurements due to the position of the accelerometer. Future analyses and studies will be devoted to the improvements on the device and the data interpretation procedure to fix some of the issues that have been found.

CRediT authorship contribution statement

Valerio De Biagi: Writing – original draft, Writing – revised manuscript, Methodology, Investigation, Formal analysis, Conceptualization. **Maddalena Marchelli:** Writing – original draft, Writing – revised manuscript, Methodology, Investigation, Conceptualization.

Declaration of competing interest

The authors declare that the do not have any conflict of interests.

Data availability

Data will be made available on request.

References

[1] Lu Y, Zhang L. Analysis of failure of a bridge foundation under rock impact. Acta Geotech 2012;7:57–68.

[2] Lu Y, Zhang L. Progressive collapse of a drilled-shaft bridge foundation under vessel impact. Ocean Eng 2013;66:101–12.

[3] Malek MAA, Rashid RS, Shukri AA, El-Zeadani M. Experimental study of impact loading effect on bridge substructures including piles. Structures 2021;31:419–27.

[4] Caredda G, Makoond N, Buitrago M, Sagaseta J, Chryssanthopoulos M, Adam JM. Learning from the progressive collapse of buildings. Dev Built Environ 2023;15:100194.

[5] Sunder S, Gann R, Grosshandler W, Lew H, et al. Final report on the collapse of the world trade center towers. Technical report, National Institute of Standards and Tecnology; 2005.

[6] Lam NT, Yong AC, Lam C, Kwan JS, Perera JS, Disfani MM, et al. Displacement-based approach for the assessment of overturning stability of rectangular rigid barriers subjected to point impact. J Eng Mech 2018;144:04017161.

[7] Kœchlin P, Potapov S. Classification of soft and hard impacts—application to aircraft crash. Nucl Eng Des 2009;239:613–8.

[8] Zhang C, Gholipour G. Concrete structures subjected to impact and blast loadings and their combinations. CRC Press; 2022.

[9] Sugano T, Tsubota H, Kasai Y, Koshika N, Orui S, Von Riesemann W, et al. Full-scale aircraft impact test for evaluation of impact force. Nucl Eng Des 1993;140:373–85.

[10] Xu X, Zhang H, Du X, Liu Q. Vehicle collision with rc structures: A state-of-the-art review. Structures 2022;44:1617–35.

[11] Mougin J-P, Perrotin P, Mommessin M, Tonnelo J, Agbossou A. Rock fall impact on reinforced concrete slab: an experimental approach. Int J Impact Eng 2005;31:169–83.

[12] Majeed ZZ, Lam NT, Lam C, Gad E, Kwan JS. Contact force generated by impact of boulder on concrete surface. Int J Impact Eng 2019;132:103324.

[13] AuYeung S, Alipour A. Evaluation of aashto suggested design values for reinforced concrete bridge piers under vehicle collisions. Transp Res Rec 2016;2592:1–8.

[14] Wittel FK, Carmona HA, Kun F, Herrmann HJ. Mechanisms in impact fragmentation. Int J Fract 2008;154:105–17.

[15] Zhao D-B, Yi W-J, Kunnath SK. Numerical simulation and shear resistance of reinforced concrete beams under impact. Eng Struct 2018;166:387–401.

[16] Ventura A, De Biagi V, Chiaia B. Effects of rockfall on an elastic–plastic member: A novel compliance contact model and dynamic response. Eng Struct 2017;148:126–44.

[17] Abrate S. Modeling of impacts on composite structures. Compos Struct 2001;51:129–38.

[18] Delhomme F, Mommessin M, Mougin J, Perrotin P. Simulation of a block impacting a reinforced concrete slab with a finite element model and a mass–spring system. Eng Struct 2007;29:2844–52.

[19] Fujikake K, Li B, Soeun S. Impact response of reinforced concrete beam and its analytical evaluation. J Struct Eng 2009;135:938–50.

[20] Wang X-H, Jing W, Zhang W-B, Wang J-H, Yun Q-L, Wang Y-Q, et al. An analysis of impact load and fragmentation dimension to explore energy dissipation patterns in coal crushing. Sci Rep 2023;13:18255.

[21] Dyskin AV, Pasternak E, Qi C, Xia C, Qu X. A possible mechanism of failure in dynamic uniaxial compression and the size effect. Eng Fract Mech 2021;257:108005.

[22] Wu M, Zhang C, Chen Z. Drop-weight tests of concrete beams prestressed with unbonded tendons and meso-scale simulation. Int J Impact Eng 2016;93:166–83.

[23] Wu M, Chen Z, Zhang C. Determining the impact behavior of concrete beams through experimental testing and meso-scale simulation: I. drop-weight tests. Eng Fract Mech 2015;135:94–112.

[24] Gili J, Ruiz-Carulla R, Matas G, Moya J, Prades A, Corominas J, et al. Rockfalls: Analysis of the block fragmentation through field experiments. Landslides 2022;19:1009–29.

[25] Li Q, Reid S, Wen H, Telford A. Local impact effects of hard missiles on concrete targets. Int J Impact Eng 2005;32:224–84.

[26] Haug ØT, Rosenau M, Leever K, Oncken O. On the energy budgets of fragmenting rockfalls and rockslides: Insights from experiments. J Geophys Res: Earth Surface 2016;121:1310–27.

[27] Sun J, Lam N, Zhang L, Ruan D, Gad E. A note on hunt and crossley model with generalized visco-elastic damping. Int J Impact Eng 2018;121:151–6.

[28] Sun J, Lam N, Zhang L, Ruan D, Gad E. Contact forces generated by hailstone impact. Int J Impact Eng 2015;84:145–58.

[29] Lam C, Yong AC, Kwan JS, Lam NT. Overturning stability of l-shaped rigid barriers subjected to rockfall impacts. Landslides 2018;15:1347–57.

[30] Yong AC, Lam NT, Menegon SJ. Collision actions on structures. CRC Press; 2022.

[31] Kiakojouri F, De Biagi V, Chiaia B, Sheidaii MR. Strengthening and retrofitting techniques to mitigate progressive collapse: A critical review and future research agenda. Eng Struct 2022;262:114274.

[32] Kishi N, Mikami H, Matsuoka K, Ando T. Impact behavior of shear-failure-type rc beams without shear rebar. Int J Impact Eng 2002;27:955–68.

[33] Zineddin M, Krauthammer T. Dynamic response and behavior of reinforced concrete slabs under impact loading. Int J Impact Eng 2007;34:1517–34.

[34] Do TV, Pham TM, Hao H. Dynamic responses and failure modes of bridge columns under vehicle collision. Eng Struct 2018;156:243–59.

[35] Demartino C, Wu J, Xiao Y. Response of shear-deficient reinforced circular rc columns under lateral impact loading. Int J Impact Eng 2017;109:196–213.

[36] Li H, Chen W, Hao H. Factors influencing impact force profile and measurement accuracy in drop weight impact tests. Int J Impact Eng 2020;145:103688.

[37] Caviezel A, Demmel SE, Ringenbach A, Bühler Y, Lu G, Christen M, Dinneen CE, Eberhard LA, von Rickenbach D, Bartelt P. Reconstruction of four-dimensional rockfall trajectories using remote sensing and rock-based accelerometers and gyroscopes. Earth Surface Dyn 2019;7:199–210.

[38] Chopra AK. Dynamics of structures: theory and applications to earthquake engineering. Pearson; 2011.

[39] Huang NE, Shen Z, Long SR, Wu MC, Shih HH, Zheng Q, Yen N-C, Tung CC, Liu HH. The empirical mode decomposition and the hilbert spectrum for nonlinear and non-stationary time series analysis. Proc R Soc A 1998;454:903–95.

[40] Daubechies I, Lu J, Wu H-T. Synchrosqueezed wavelet transforms: An empirical mode decomposition-like tool. Appl Comput Harmon Anal 2011;30:243–61.

[41] Dragomiretskiy K, Zosso D. Variational mode decomposition. IEEE Trans Signal Process 2013;62:531–44.

[42] Massouleh SM, Kordkheili SH. Experimental investigation of empirical mode decomposition by reduction of end effect error. Phys A 2019;534:122171.

[43] Rato R, Ortigueira MD, Batista A. On the hht, its problems, and some solutions. Mech Syst Signal Process 2008;22:1374–94.

[44] Dätig M, Schlurmann T. Performance and limitations of the hilbert–huang transformation (hht) with an application to irregular water waves. Ocean Eng 2004;31:1783–834.

[45] Carmona HA, Wittel FK, Kun F, Herrmann HJ. Fragmentation processes in impact of spheres. Phys Rev E 2008;77:051302.

[46] Guccione DE, Buzzi O, Thoeni K, Fityus S, Giacomini A. Predicting the fragmentation survival probability of brittle spheres upon impact from statistical distribution of material properties. Int J Rock Mech Min Sci 2021;142:104768.

[47] Wu S, Chau KT, Yu T. Crushing and fragmentation of brittle spheres under double impact test. Powder Technol 2004;143:41–55.

[48] Alves M, Oshiro RE. Scaling the impact of a mass on a structure. Int J Impact Eng 2006;32:1158–73.

[49] Mazzariol L, Oshiro R, Alves M. A method to represent impacted structures using scaled models made of different materials. Int J Impact Eng 2016;90:81–94.

[50] Mazzariol LM, Alves M. Experimental verification of similarity laws for impacted structures made of different materials. Int J Impact Eng 2019;133:103364.

[51] Korsunsky A, Warren P, Hills D. Impact fracture thresholds in brittle solids. Wear 1995;186:99–104.

[52] Oshiro RE, Alves M. Scaling impacted structures. Archive of applied mechanics 2004;74:130–45.

[53] Wang Y, Liang D, Xi X, Wang J, Liu X, He H. Prediction techniques for the scaled models made of different materials under impact loading. Int J Impact Eng 2023;179:104642.

[54] Davey K, Darvizeh R, Zhang J. Finite similitude in fracture mechanics. Eng Fract Mech 2021;245:107573.

[55] Zhou C, Xu C, Karakus M, Shen J. A particle mechanics approach for the dynamic strength model of the jointed rock mass considering the joint orientation. Int J Numer Anal Methods Geomech 2019;43:2797–815.

[56] Starossek U. Progressive collapse of structures. 2nd ed. London, UK: ICE Publishing; 2018.

[57] Mavrouli O, Giannopoulos P, Carbonell JM, Syrmakezis C. Damage analysis of masonry structures subjected to rockfalls. Landslides 2017;14:891–904.